Thermodynamic determination and assessment of the CsF-ThF_4 system

Vozárová, N.; Smith, A. L.; Colle, J-Y; Raison, Philippe E.; Bouëxière, D.; Konings, R. J.M.; Beneš, O.

DOI
10.1016/j.jct.2017.05.008

Publication date
2017

Document Version
Final published version

Published in
The Journal of Chemical Thermodynamics

J. Chem. Thermodynamics 114 (2017) 71–82

Contents lists available at ScienceDirect

J. Chem. Thermodynamics

journal homepage: www.elsevier.com/locate/jct

Thermodynamic determination and assessment of the CsF-ThF_4 system

N. Vozárová [a,b,*], A.L. Smith [c], J-Y. Colle [a], P.E. Raison [a], D. Bouëxière [a], R.J.M. Konings [a,c], O. Beneš [a]

[a] Joint Research Centre (JRC), Directorate G, Nuclear Safety and Security, European Commission, P.O. Box 2340, 76125 Karlsruhe, Germany
[b] Swiss Federal Institute of Technology (ETH), Department of Mechanical and Process Engineering, Rämistrasse 101, 8092 Zürich, Switzerland
[c] Delft University of Technology, Faculty of Applied Sciences, Department of Radiation Science & Technology, Nuclear Energy and Radiation Applications (NERA), Mekelweg 15, 2629 JB Delft, The Netherlands

ARTICLE INFO

Article history:
Received 31 December 2016
Received in revised form 4 May 2017
Accepted 5 May 2017
Available online 9 May 2017

Keywords:
Molten salt reactor
Phase equilibria
Vapour pressure
Nuclear fuel safety
Fluorides
Thermodynamics

ABSTRACT

In this study we present a comprehensive thermodynamic description of the binary CsF-ThF_4 system. The phase equilibria of several intermediate compositions in this system have been determined using the DSC technique combined with a post-analysis using powder X-ray diffraction. Considering all the novel experimental data, a thermodynamic model for the CsF-ThF_4 system has been developed for the first time using the Calphad approach. The present model reproduces very well the measurements performed. Knudsen effusion mass spectrometry (KEMS) has further been used to investigate the vapour pressure over the molten CsF-ThF_4 salt and to determine the thermodynamic activities of CsF and ThF_4 in the liquid solution. As part of this study, the vaporization of pure CsF was examined and the results were compared with the literature showing a good agreement. Next, the vapour pressure of CsF-ThF_4 in the liquid solution was investigated by measuring three samples with compositions X ThF_4 = (0.4, 0.6, 0.8) mol/mol. A strong negative deviation from Raoult's law was observed for both species, more evident in case of CsF, and a good agreement with the predictions of our thermodynamic model was found. This article is a prerequisite for the assessment of the ternary LiF-CsF-ThF_4 system.

1. Introduction

The molten salt reactor (MSR) was selected along with 5 other concepts as one of the most promising nuclear reactor types for the future fission reactor technologies by the Generation IV International Forum [1]. The nuclear fuel in this design is dissolved in a carrier salt and circulated in the core, therefore omitting the need for fuel rods and allowing higher temperature and therefore higher thermal efficiency. In addition, the design can be coupled with a thorium fuel cycle for a sustainable energy production, thorium being three times more abundant on Earth than uranium [2]. Current research efforts in Europe are focused on a $^{7}LiF\text{-}ThF_4 - UF_4 - PuF_3$ liquid fuel for a fast spectrum reactor [3]. The present work reports the description of the CsF-ThF_4 system as ^{137}Cs is one of the major fission products, with a high yield of 7% [4]. Cesium has a high contribution to the environmental burden in case of a nuclear accident, and its potential release into the environment is a subject of primary concern for the safety of the general public. The knowledge of the phase equilibria during normal operating and off-normal conditions, and a thorough understanding of the release mechanism of cesium from the salt are therefore crucial. The vapour pressure indeed determines the driving force for radioactivity release in case of an accident with uncontrolled temperature increase. Furthermore, the reactor salt is a multi-component salt, optimised to have a lowest liquidus temperature in order to avoid freezing. Any higher evaporation of a component with respect to the others would lead to a change in composition of the fuel mixture and therefore change in its thermodynamic properties. An increase of the melting point could occur, which would result in lowering or even crossing of the safety margin. The only experimental data available to this date for the CsF-ThF_4 system are the phase diagram data of Thoma and Carlton [5] and the structural studies of the $CsThF_5$, $CsTh_3F_{13}$ and $CsTh_6F_{25}$ intermediate compounds by Underwood et al. [35,36,37].

The present work reports for the first time a complete thermodynamic assessment of the CsF-ThF_4 binary system, including phase diagram data, vapour pressures, and thermodynamic activities of the liquid solution using differential scanning calorimetry (DSC), X-ray diffraction (XRD) and Knudsen effusion mass spectrometry (KEMS). In addition, the experimental measurements have been used to develop a thermodynamic model for this system using the Calphad method [28,29].

* Corresponding author at: Institute for nuclear waste disposal (INE), Hermann-von-Helmholtz-Platz 1, D-76344 Eggenstein-Leopoldshafen, Germany.
E-mail addresses: nikoleta.vozarova@kit.edu (N. Vozárová), ondrej.benes@ec.europe.eu (O. Beneš).

http://dx.doi.org/10.1016/j.jct.2017.05.008
0021-9614/

2. Experimental methods

2.1. Sample preparation

All samples were handled inside the dry atmosphere of an argon-filled glove box because of their high sensitivity to water and oxygen. The oxygen and moisture impurity content in this box was long-term under 1 ppm for oxygen and under 2 ppm for water. Samples of various compositions of the CsF-ThF_4 system were prepared from commercial CsF and in-house prepared ThF_4 end-members. The ThF_4 material was synthesized from oxide by the fluorination process at 873.15 K under argon flow. The thorium dioxide was obtained from thorium nitrate solution (available from JRC-Karlsruhe stock) by precipitation of thorium by oxalic acid, filtration of the formed oxalate and further thermal decomposition and conversion into oxide at 1073.15 K for 4 h under dynamic air atmosphere [6]. The conversion of oxides into fluorides is achieved by use of pure HF gas, where the following reaction is taking place [7].

$$ThO_2 + 4HF \rightarrow ThF_4 + 2H_2O \quad (1)$$

The purity of the starting material was assessed using differential scanning calorimetry and X-ray diffraction. The result obtained for ThF_4 (T_M = 1385.65 K) was in close agreement with the literature data (T_M = 1384.15 K) [8] confirming high purity of the starting material. To remove residual moisture from the commercial CsF, a drying procedure was applied for several hours at 673 K under argon flow using the flow rate of 0.5 L/min at 1 bar. The provenance and purity of the starting materials is shown in Table 1.

2.2. Differential scanning calorimetry

The melting points and the phase equilibria points were examined using the differential scanning calorimeter (DSC) detector of type SETARAM MDHTC96. The equipment consists of a furnace for heating and a detector for the measurement of the heat flow difference between sample and reference crucible. The reference crucible is kept empty and both crucibles are surrounded by a series of S-type thermocouples [9,10].

The alkali fluoride vapours become very corrosive at elevated temperatures and in order to avoid the damage to the platinum thermocouples in the calorimetric device, the encapsulation technique based on stainless steel crucible with inert Ni liner developed at JRC-Karlsruhe was used [11]. The whole experimental chamber is under argon atmosphere in order to avoid oxidation of the stainless steel container at high temperatures. Calibration of the temperature was applied to all measurements performed by DSC to compensate for the thermal gradient and time delay caused by the penetration of the heat through the crucible wall to the sample during the dynamic regime. The most frequent DSC calibrants are metals with high purity of known melting temperatures. Indium, aluminium, gold, lead, silver, copper, zirconium and tin were chosen as calibrants since they all have different melting points. These standard materials have been heated up at different rates from 2 K/min to 12 K/min, the melting temperatures have been measured and the difference between the measured and the theoretical melting temperature has been plotted as a function of the heating rate. These points were then fitted with a linear fit. The intercept and slope of this fit were further plotted as a function of the melting temperatures for all calibrants and fitted to obtain the full calibration relation.

The DSC measurements consisted of two cycles with 10 K/min heating ramp up to 1473 K, and successive cooling down to 373 K, with cooling rate of 10 K/min. The phase equilibria data were derived from the onset temperature from the second cycle, the first cycle allowing mixing of the end-members in the appropriate ratios. The DSC has a low uncertainty of ± 2 K, however, due to weak signals, the standard uncertainty on the temperature for the phase equilibria measurements was estimated to be ± 10 K.

2.3. Powder X-ray diffraction

The intermediate compound compositions in the CsF-ThF_4 phase diagram were characterized at room temperature by X-ray diffraction after the successive cycles in the DSC. The measurements were carried out using a Bruker D8 Bragg–Brentano X-ray diffractometer mounted inside a glovebox and equipped with a curved Ge monochromator (111), a copper tube (40 kV, 40 mA), and a LinxEye position sensitive detector. The data were collected by step scanning in the range $10° < 2\theta < 120°$, with an integration time of about 8 h, a count step of 0.02° (2θ), and a dwell of 5 s/step. Structural analysis was performed using the Powder Cell software (Version 2.4) and by Le Bail fit using the Fullprof2k suite [12].

2.4. Knudsen effusion mass spectrometry

Knudsen Effusion Mass spectrometry (KEMS) is a powerful tool for the determination of the thermodynamic properties at high temperatures based on the equilibrium between condensed and gaseous phases. It can be used for identification of the gas composition and its vaporising behaviour as a function of temperature by means of the conversion of the detected spectral ion intensity data into the corresponding vapour pressures of the species in the gaseous phase. This method can further be used for determination of other thermodynamic properties such as sublimation enthalpies, thermodynamic activities, and ionisation energies of gaseous species.

The KEMS apparatus used in this study is installed in a glove box to permit the handling of radioactive materials. The only commercially obtained part of the apparatus is the mass spectrometer. The KEMS system consists of a Knudsen effusion cell with tungsten crucible, which is placed in a vacuum chamber (10^{-6} -10^{-7} mbars), coupled to a QMG 422 quadrupole mass spectrometer from Pfeiffer Vacuum. Within the cell, in which the sample and the reference material are placed, the equilibrium is achieved between the gas and condensed phases. The cell is heated by tungsten coil heating elements under constant rate, while appropriate thermal insulation is achieved by tungsten shields. The cell temperature is externally controlled by a IMPAC IS12 pyrometer calibrated prior to the experiment based on melting points of known standard metals (Cu, Pt, Ag) showing at that point a plateau on the MS intensity curve. The uncertainty of the pyrometer is ±10 K [13,14]. Tungsten was chosen for the furnace heating elements as well as the material of the crucible due to its high melting point and negligible reactivity with the sample. The beam of

Table 1
The provenance and purity of all materials used in this study. DSC: Differential scanning calorimetry, XRD: X-ray diffraction.

Material	Supplier	Initial Weight Fr. Purity	Purification Method	Final Weight Fr. Purity	Analysis Method
CsF	Alfa Aesar	0.999	Drying	0.999	–
ThF_4	In-house made	–	Fluorination	0.999	DSC/XRD

gaseous species then exits the cell through the small effusion orifice at the top of the cell and is further ionized with a cross beam electron bombardment ion source. The formed ions are then accelerated in the electric field and separated in the magnetic field. The separation of the species is due to the different mass to charge ratios of the species. The experimental setup is displayed in Fig. 1.

Secondary electron multiplier detector connected to the mass spectrometer allows ion current measurements and analysis of the mass spectrum of the beam and provides the intensities of ion currents of the evaporated species. The range of the mass spectrometer is 1–512 amu. Every measurement was performed using a constant heating rate of 10 K/min and applying an electron ionisation energy of 33.5 eV. The sample and the reference material were heated until complete evaporation, which is indicated by a sharp signal drop. Furthermore, an analog scan was done to detect other masses in case of the reaction between tungsten or silver and arising species as well as between species arising from the sample. Since none of the corresponding masses for the reaction between silver/tungsten and arising species were detected, it shows that no unexpected reactions took place during the measurement. For the CsF end-member, the electron-fragmentation processes were identified by appearance potential measurements. This measurement was performed at a constant temperature with increasing electron energy from 2 eV to 63.5 eV with a step of 0.5 eV. For the ThF_4 end-member the electron-fragmentation processes were taken from our earlier work by Capelli et al. [15].

2.4.1. Mass spectral analysis

The conversion of the mass spectrometric signal into the vapour pressure of the molecular species P_i is done according to the following relation [16]:

$$P_i = \frac{(I_i^+ \cdot T)}{K}, \tag{2}$$

in which P_i is the partial pressure, T is the absolute temperature and I_i^+ is the intensity of the measured mass spectrometric signal of species i. K stands for a calibration factor, which includes the silver calibration factor, K_{Ag}, and a correction factor dependent on species i, K_i.

$$K = K_{Ag} \cdot K_i \tag{3}$$

The silver calibration factor is determined based on the vaporization of a known quantity of silver, which is placed inside the cell together with the sample, by comparing with the well-known pressure data from Margrave and Hultgren [17].

$$K_{Ag} = \frac{(T \cdot I_{Ag}^+)}{P_{Ag}} \tag{4}$$

The species dependent factor is defined as follows:

$$K_i = \frac{\sigma_i}{\sigma_{Ag}} \cdot \frac{\gamma_i}{\gamma_{Ag}}, \tag{5}$$

in which σ_{Ag} and σ_i are the electron impact ionization cross sections of silver and species i, respectively, and γ_i/γ_{Ag} is the ratio of normalised secondary electron multiplier (SEM) efficiency. The secondary electron multiplier efficiency as suggested by Grimley et al. [18] is approximated as:

$$\gamma_i = \frac{\delta}{\sqrt{M_i}}, \tag{6}$$

in which δ is a constant. The SEM ratio can subsequently be expressed as:

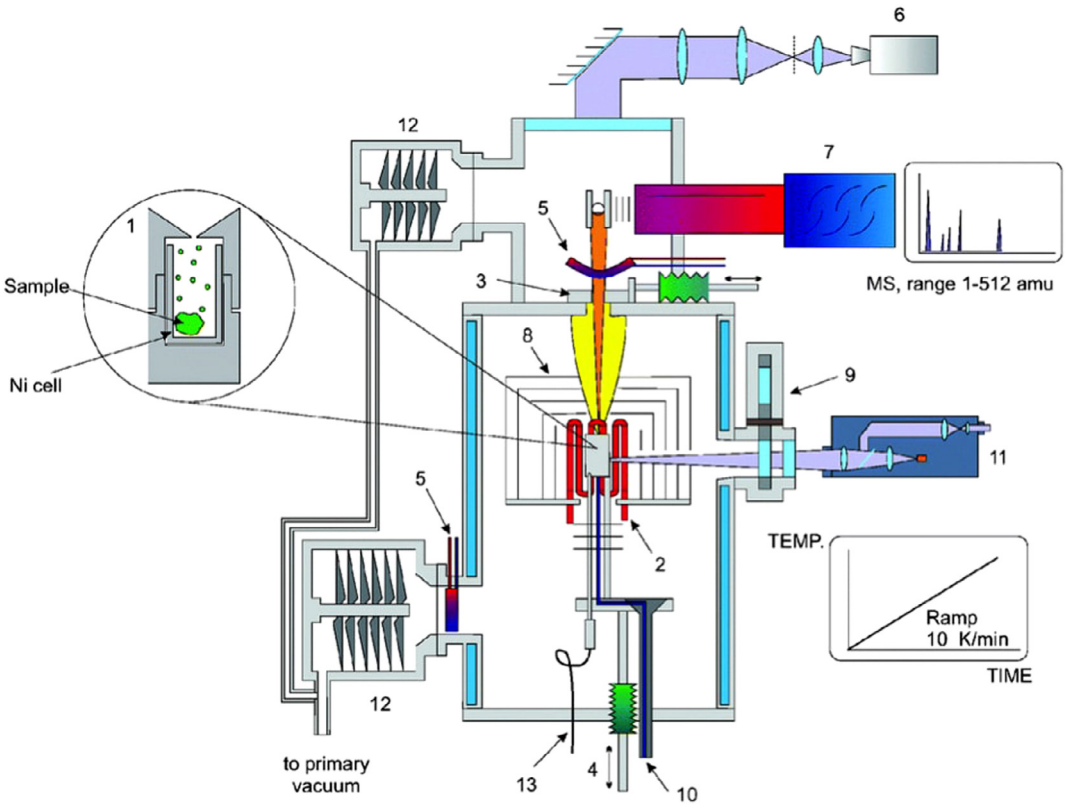

Fig. 1. The KEMS experimental setup used in this study, (1) Knudsen cell with sample, in W cell, (2) Tungsten heating coil, (3) Molecular beam chopper, (4) Cell lift facilities for fast heating or cooling, (5) Liquid nitrogen trap to reduce background signal, (6) Camera to align the cell holder and chopper diaphragm, (7) Quadrupole mass spectrometer, (8) Thermal shield, (9) Revolving protection windows, (10) Inlet gas capillary, (11) Linear pyrometer, (12) Turbo molecular pump, (13) Removable W/Re thermocouple. The orifice diameter is 0.5 mm, and the length is 0.25 mm.

$$\frac{\gamma_i}{\gamma_{Ag}} = \frac{\sqrt{M_{Ag}}}{\sqrt{M_i}}, \tag{7}$$

where M_{Ag} and M_i are the molar masses of silver and species i respectively. This relationship is, however, only valid for mass numbers greater than 50 amu, which is verified for all species monitored in this work.

The vapour flux of silver, escaping from the orifice was obtained from the Hertz-Knudsen-Langmuir equation:

$$\frac{dm}{dt} = P_{Ag} \cdot S \cdot C \cdot \frac{\sqrt{M_{Ag}}}{\sqrt{2\pi RT}}, \tag{8}$$

where dm/dt is the mass loss rate of silver, M_{Ag} is the molecular weight of the escaping silver vapor, R is the universal gas constant, T is the absolute temperature, S is the effusion orifice surface and C is the Clausing factor accounting for the shape of the effusion orifice.

Combining Eqs. (4) and (8), the corresponding mass loss G_i over the Δt duration can be expressed as follows:

$$G_i(\Delta t) = I^+_{Ag} \cdot S \cdot C \cdot \Delta t \cdot \sqrt{M_{Ag}} \cdot \frac{1}{\sqrt{2\pi R}} \cdot \frac{\sqrt{T}}{K_{Ag}} \tag{9}$$

The total mass effused can, therefore, be determined as the sum of the G_i over the period of effusion. Applying the latter equation to silver, the silver calibration factor is obtained and compared to the determination based on the vapour pressure data only. This approach was used to estimate the uncertainty on the absolute pressure values, which, averaged from all measurements gives $\Delta P = \pm 0.046$ Pa at T = 1050 K for ThF_4, $\Delta P = \pm 0.15$ Pa at T = 1050 K for CsF, $\Delta P = \pm 2.95$ Pa at T = 1300 K for ThF_4 and $\Delta P = \pm 4.8$ Pa at T = 1300 K for CsF. Overall, both approaches provide similar values of vapour pressures.

2.4.2. Ionization cross sections

As mentioned in the previous section (Eq. (5)), one of the key parameters for the calculation of vapour pressures from KEMS data is the ionization cross section. This cross section depends on the ionization energy, e.g., the energy of the ion impact electron source. Ionization cross sections for atoms have been estimated by Mann [19], and these were calculated in this work at the ionization energy of the measurement using the software Sigma [20,21]. The calculation of the cross sections for molecular species is more challenging, however. The approach of Otvos and Stevenson [22] using the simple sum of the respective atomic cross sections leads to discrepancies with experimental observations, especially for complex molecules. Deutsch et al. [24] have presented an alternative approach which considered weighting factors to account for the contribution of each constituent atom depending on its atomic radius and effective number of atomic electrons. For a molecule of the type AB_n, the modified additivity rule of Deutsch et al. [24] is expressed in Eq. (10) below:

$$\sigma^+(AB_n) = [(r_A^2)/(r_B^2)]^{\alpha} \cdot [\xi_A/(\xi_A + n\xi_B)] \cdot \sigma_A^+ + [(nr_B^2)/(r_A^2)]^{\beta} \cdot [n\xi_b/(\xi_A + n\xi_B)] \cdot n\sigma_B^+, \tag{10}$$

in which r_A and r_B are the atomic radii listed in the table of Desclaux [23], σ_A^+ and σ_B^+ are the atomic ionization cross sections taken from the Sigma software at the ionization energy of the measurement (in this case, 33.5 eV). The exponents α and β are dependent on all of the above parameters and were obtained empirically [24]. ξ_A and ξ_B correspond to the effective number of atomic electrons and these values have been established according to the orbital configurations and number of electrons, which can be released from the shell depending on the ionization energy of the measurement for each atom [25,26,27].

3. Thermodynamic modelling

The phase diagram assessment was performed using the thermodynamic data obtained in this study by the DSC technique combined with XRD analysis of the heated samples. The optimization was done with the Factsage software using the Calphad method [28,29]. An assessment of a phase diagram requires knowledge of the Gibbs energy of all phases considered in the system including compounds and solutions.

3.1. Pure compounds

For pure compounds, the Gibbs energy function is defined as:

$$G(T) = \Delta_f H^0(298.15K) + \int_{298.15}^{T} Cp(T)dT - T \cdot \left(S^0(298.15K) + \int_{298.15}^{T} \frac{Cp(T)}{T} dT\right), \tag{11}$$

in which T is the absolute temperature, S^0 (298.15 K) is the standard absolute entropy at the reference temperature, $\Delta_f H^0$ (298.15 K) is the standard enthalpy of formation at the reference temperature and C_p(T) is the heat capacity as a function of the temperature. The thermodynamic data of the numerous intermediate compounds in the CsF-ThF_4 phase diagram were not known in contrast to the pure end components, and therefore have been optimized during the phase diagram assessment. The enthalpy of formation and absolute entropy (both at 298.15 K) of intermediate compounds were optimized, while heat capacities were estimated based on the Neumann–Kopp rule [30]. The final optimized data for the intermediate phases plus the heat capacities calculated from end-members are shown in Table 2.

3.2. Liquid solution

No solid solutions stabilize in the CsF-ThF_4 system and the only solution phase was the liquid. The Gibbs energy function of a solution is described as:

$$G_{sol}(T) = G_A(T) \cdot x_A + G_B(T) \cdot x_B + R \cdot T \cdot (x_A \ln x_A + x_B \ln x_B) + \Delta G_{excess}, \tag{12}$$

in which x_A and x_B are the mole fractions of mixed end-members, G_A (T) and G_B (T) are temperature functions of the molar Gibbs energies of the end-members, R is the universal gas constant and ΔG_{excess} is the excess Gibbs energy function. The description of the liquid solution of the modelled CsF –ThF_4 system was performed using the modified quasichemical model [31], which is used in the JRC-Karlsruhe database for fluoride salts. The excess parameter for the Gibbs energy described in this model developed by Pelton et al. [31] is the Gibbs energy change $\Delta g_{CsTh/F}$ for second nearest neighbour (SNN) pair exchange reaction in a quasi-lattice indicated by Eq. 13. First nearest neighbours correspond to cation–anion pair exchange, whereas SNN correspond to cation-cation pair exchange.

$$(Cs - F - Cs) + (Th - F - Th) = 2 \cdot (Cs - F - Th) \tag{13}$$

The $\Delta g_{CsTh/F}$ parameter can be expanded in form of polynomials, for the specific system of interest as follows:

$$\Delta g_{CsTh/F} = \Delta g^0_{CsTh/F} + \sum\nolimits_{i+j \geqslant 1} g^{ij}_{CsTh/F} \cdot Y^i_{CsTh/F} \cdot Y^j_{ThCs/F}, \tag{14}$$

in which $\Delta g^0_{CsTh/F}$ and $g^{ij}_{CsTh/F}$ are coefficients obtained from the optimisation of the CsF –ThF_4 binary liquid solution. $Y^j_{ThCs/F}$ stands for the composition dependent coordination equivalent fraction and can be expressed as shown below:

Table 2
Thermodynamic data for pure and intermediate compounds used in this work for the phase diagram assessment. Data for gaseous species used for calculating the vapour pressure are given as well. $\Delta_f H^0$ (298.15 K) stands for the standard enthalpy of formation at the reference temperature, ΔH trans. is the transition enthalpy, S^0 (298.15 K) is the standard absolute entropy at the reference temperature, a–g are the heat capacity coefficients and T is the absolute temperature in K.

Compound	$\Delta_f H^0$ (298.15 K)/ (J·mol^{-1})	ΔH trans./ (J·mol^{-1})	S^0 (298.15 K)/ (J·K^{-1}·mol^{-1})	a	bT	cT^2	dT^{-2}	eT^3	fT^4	gT^{-1}	References
ThF_4(s)	−2100000	–	142.05	122.17	0.00837	-	−1260000	–	–	–	[32]
ThF_4(l)	−2103654	41800 at 1383 K	101.24	170.00	–	–	–	–	–	–	[32]
ThF_4(g)	−1748200	–	351.56	122.4	−0.014064	$7.3654E^{-6}$	–	$-1.9394E^{-9}$	$2E^{-13}$	−7544.55	[33]
CsF(s)	−555000	–	93.60	24.29	0.06460	–	590000	–	–	–	[33 34]
CsF(l)	−534714	22100 at 973 K	108.19	70.56	–	–	–	–	–	–	[33 34]
CsF(g)	−356500	–	243.21	37.38	0.00057	–	−157081	–	–	–	[33]
Cs_2F_2(g)	−891859	-	358.056	83.101	$2.2E^{-5}$	$-3E^{-9}$	−302800	–	–	–	[33]
Cs_3ThF_7(s)	−3870476	-	456.00	195.05	0.20200	–	515000	–	–	–	This work
Cs_2ThF_6(s)	−3269400	–	372.40	170.76	0.13800	–	−75000	–	–	–	This work
$CsThF_5$-α(s)	−2722900	–	225.20	146.46	0.07300	–	−665000	–	–	–	This work
$CsThF_5$-β(s)	−2710900	12000 at 942 K	237.93	146.46	0.07300	-	−665000	–	–	–	This work
$Cs_2Th_3F_{14}$(s)	−7555000	–	593.00	415.10	0.15400	–	−2590000	–	–	–	This work
$CsTh_2F_9$(s)	−4818625	–	376.57	268.64	0.08130	–	−1920000	–	–	–	This work
$CsTh_3F_{13}$(s)	−6940048	–	501.14	390.81	0.08970	–	−3180000	–	–	–	This work
$CsTh_6F_{25}$(s)	−13230900	–	939.42	757.33	0.11500	–	−6940000	–	–	–	This work

$$Y_{ThCs/F} = \frac{(X_{ThCs})}{(X_{CsCs} + X_{ThCs} + X_{ThTh})}, \quad (15)$$

in which X_{AB} stands for a cation-cation pair mole fraction.

These mole fractions are furthermore related to the coordination numbers $Z^{Cs}_{CsTh/FF}$ and $Z^{Th}_{CsTh/FF}$, which are taken in this model at the point of the maximum SNN short range ordering. In order to maintain the electroneutrality, the anion-anion coordination numbers are calculated as follows:

$$\frac{q_{Cs}}{Z^{Cs}_{CsTh/FF}} + \frac{q_{Th}}{Z^{Th}_{CsTh/FF}} = \frac{q_F}{Z^{F}_{CsTh/FF}} + \frac{q_F}{Z^{F}_{CsTh/FF}}, \quad (16)$$

in which $q_{Cs,Th,F}$ is the absolute charge for the different ions, which in this case are 1, 4 and −1, respectively. Values used for the coordination numbers are listed in Table 3.

Combining all above, the optimized excess parameter is expressed in Eq. 17.

$$\Delta g_{CsTh/F} = -39329,6 - 11234 \cdot Y_{CsTh/F} + 2928,8 \cdot Y_{ThCs/F}\ (\mathrm{J \cdot mol^{-1}}) \quad (17)$$

4. Results

4.1. Phase diagram data

The phase equilibria in the CsF–ThF_4 system were measured experimentally to serve as input for the phase diagram assessment. The only experimental data available to this date on this system are by Thoma and Carlton [5], who used thermal analysis and quenching techniques prior to X-ray characterization. The experimental data obtained in this work are listed in Table 4, together with their associated equilibria.

Table 3
Cation-Cation coordination numbers of the liquid solution. Z^A_{AB} and Z^B_{AB} are the coordination numbers, taken in this model at the point of the maximum SNN short range ordering.

A Cation	B Cation	Z^A_{AB}	Z^B_{AB}
Cs^+	Cs^+	6	6
Th^{4+}	Th^{4+}	6	6
Cs^+	Th^{4+}	3	6

Table 4
Equilibrium data of the CsF-ThF_4 system obtained by DSC in this study at pressure p = 0.1 MPa. X ThF_4 is the molar fraction of ThF_4 and T is the absolute temperature in K. The standard uncertainties u are u(X) = 0.001, u(T) = 10 K, u(p) = 10 kPa.

X ThF_4/(mol/mol)	T/K	Equilibrium type
0	972	CsF Melt. Point
0.0995	916.9	Eutectic
0.148	909.8	Eutectic
0.252	1147.7	Eutectic
0.252	1254.1	Congruent melting
0.33	1156.8	Congruent melting
0.399	947.1	α/β Transition
0.399	1057.2	Eutectic
0.4508	946.1	Eutectic
0.4508	1054.9	Eutectic
0.4508	1077.6	Liquidus
0.5	942.7	α/β Transition
0.5	1109.2	Eutectic
0.5	1132.9	Congruent melting
0.5333	939.7	α/β Transition
0.5333	1110.5	Peritectic
0.5333	1158.8	Liquidus
0.563	939.3	α/β Transition
0.563	1099.9	Peritectic
0.563	1135.0	Peritectic
0.563	1160.6	Liquidus
0.596	1116.3	Peritectic
0.596	1132.6	Peritectic
0.665	941.0	α/β Transition
0.665	941.0	or ↓ Stab. limit of $CsTh_3F_{13}$
0.665	1109.1	↓ Stab. limit of $CsTh_2F_9$
0.665	1133.7	Peritectic
0.665	1251.1	Liquidus
0.7466	1128.3	Peritectic
0.7466	1299.8	Liquidus
0.7955	1111.8	Decomposition
0.7955	1134.3	Peritectic
0.7955	1324.6	Liquidus
0.8622	1329.1	Liquidus
0.894	1323.9	Eutectic
0.9458	1328.6	Eutectic
0.9458	1359.9	Liquidus
1	1382.9	ThF_4 Melt. Point

4.2. X-ray diffraction analysis

The ($CsF:ThF_4$) = (1:6), (1:3), (1:2), (2:3), (1:1), (2:1), (3:1) compositions were analysed using powder X-ray diffraction following the DSC measurements. The corresponding X-ray diffraction patterns are compared in Figs. 2–7 to the reflections listed in the work of Thoma and Carlton [5] and to the structural models reported by Underwood et al. [35,36,37] for $CsThF_5$, $CsTh_3F_{13}$ and $CsTh_6F_{25}$ intermediate compounds.

The X-ray diffraction data for the ($CsF:ThF_4$)=(1:6), i.e., $CsTh_6F_{25}$, composition is in rather good agreement with the data of Thoma and Carlton [5]. Approximatively 96% of the Bragg reflections listed by Thoma and Carlton [5] match the experimental pattern. More recently, Underwood et al. [35] have synthesised this phase hydrothermally and solved its crystal structure: tetragonal in space group $P6_3/mmc$. A Le Bail refinement was performed using the aforementioned structural model, yielding cell parameters as $a = 8.3490(9)$ Å, $c = 16.835(2)$ Åin agreement with the literature. Very small impurities were detected, however, which could possibly correspond to ThF_4.

The XRD pattern obtained for the ($CsF:ThF_4$)=(1:3), i.e., $CsTh_3F_{13}$, composition is in very poor agreement with the data of Thoma and Carlton [5]. Only 64% of their listed reflections are found in the present XRD pattern, and a number of additional reflections are also observed. Underwood et al. [36] have recently reported two polymorphs for $CsTh_3F_{13}$, in space groups $P6/mmm$ and $Pmc2_1$ from single crystal data. But again, the experimental pattern does not match those data. The experimental pattern indicates instead a phase mixture with $Cs_2Th_3F_{14}$ and $CsTh_6F_{25}$ end-members, suggesting $CsTh_3F_{13}$ is not stable down to room temperature. This was also suggested by the small endothermic peak observed at X = 0.665 mol/mol of ThF_4 (941 K). However such transition is in a contradiction with the literature data [36], which suggests the existence of a stable phase, as well as with the remaining experimental data, as it was observed neither at X = 0.75 mol/mol of ThF_4 nor at X = 0.80 mol/mol of ThF_4. Further experimental investigations are required to solve this discrepancy.

$CsTh_2F_9$ is not stable at room temperature according to Thoma and Carlton [5]. This observation was confirmed in the present study, in which the same X-ray diffraction reflections were obtained for the ($CsF:ThF_4$) = (1:2) and ($CsF:ThF_4$) = (1:3) compositions. Upon cooling to room temperature, the $CsTh_2F_9$ phase decomposes into a phase mixture with $Cs_2Th_3F_{14}$ and $CsTh_3F_{13}$ end-members, which further decomposes into a mixture of

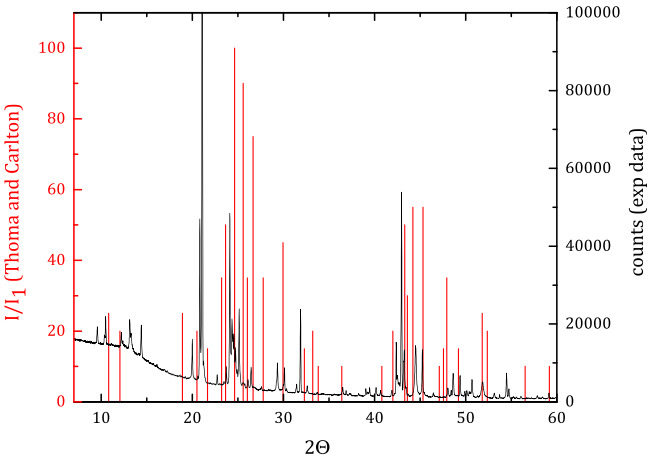

Fig. 3. Comparison between the X-ray diffraction pattern obtained in this work for the ($CsF:ThF_4$) = (1:3) composition with the reflections listed by Thoma and Carlton [5] $CsF{\cdot}3ThF_4$. Around 64% of the listed reflections match our experimental data.

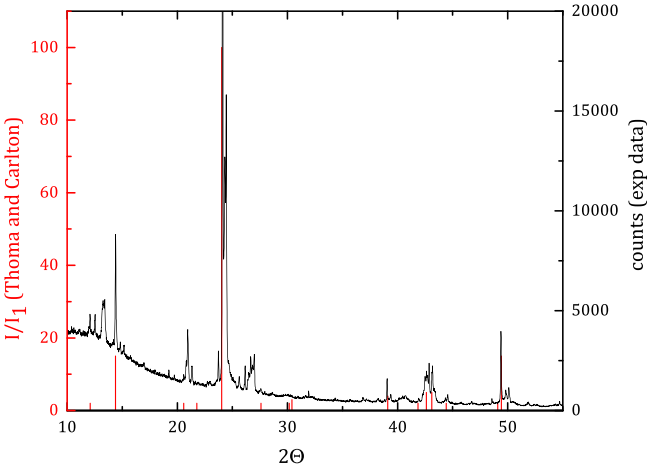

Fig. 4. Comparison between the X-ray diffraction pattern obtained in this work for the ($CsF:ThF_4$) = (2:3) composition with the reflections listed by Thoma and Carlton [5] $2CsF{\cdot}3ThF_4$. Around 67% of the listed reflections match our experimental pattern.

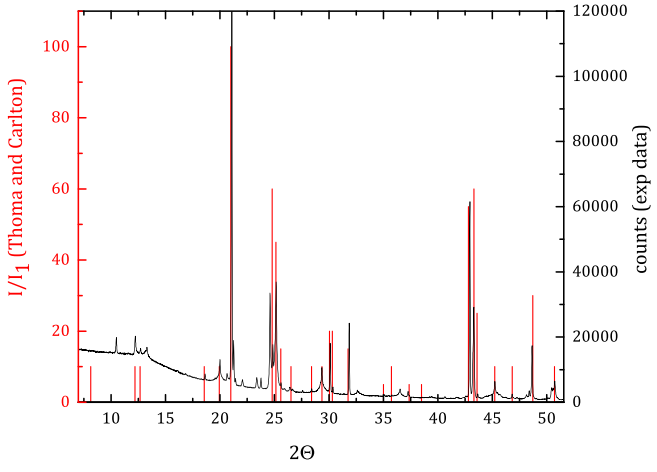

Fig. 2. Comparison between the X-ray diffraction pattern obtained in this work for the ($CsF:ThF_4$) = (1:6) composition with the reflections listed by Thoma and Carlton [5] for $CsF{\cdot}6ThF_4$. Around 96% of the listed reflections match our experimental data.

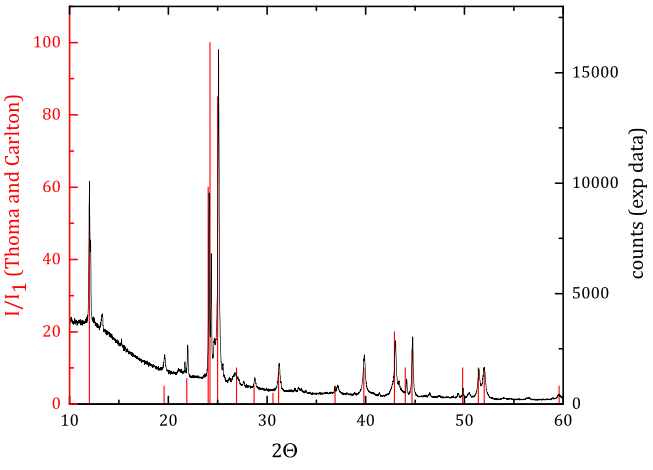

Fig. 5. Comparison between the X-ray diffraction pattern obtained in this work for the ($CsF:ThF_4$) = (1:1) composition with the reflections listed by Thoma and Carlton [5] $CsF{\cdot}ThF_4$. Around 89% of the listed reflections match our experimental pattern.

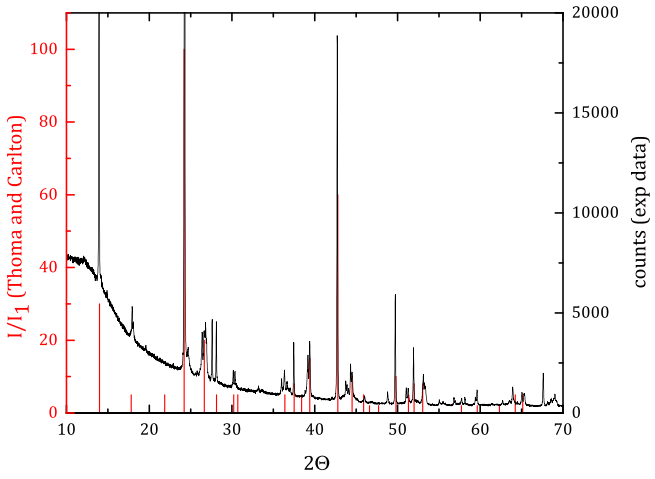

Fig. 6. Comparison between the X-ray diffraction pattern obtained in this work for the $(CsF:ThF_4) = (2:1)$ composition with the reflections listed by Thoma and Carlton [5] for $2CsF{\cdot}ThF_4$. Around 73% of the listed reflections match our experimental pattern.

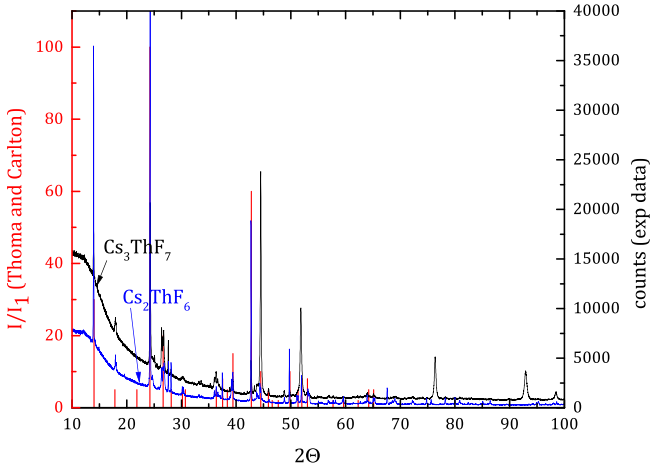

Fig. 7. Comparison between the X-ray diffraction pattern obtained in this work for the $(CsF:ThF_4) = (3:1)$ composition with the reflections listed by Thoma and Carlton [5] for $2CsF{\cdot}ThF_4$.

$Cs_2Th_3F_{14}$ and $CsTh_6F_{25}$ at room temperature according to the present XRD results.

The XRD data for the $(CsF:ThF_4) = (2:3)$, i.e. $Cs_2Th_3F_{14}$, composition is in moderate agreement with the main reflections listed by Thoma and Carlton [5]. Around 67% of the listed reflections match our experimental XRD pattern. The crystal structure for this phase was not reported in the literature, and no structural analogue could be found. The main reflections of the $CsThF_5$ phase were absent, confirming the stability of the $Cs_2Th_3F_{14}$ phase at room temperature.

The experimental pattern for the $(CsF:ThF_4) = (1:1)$, i.e., $CsThF_5$, composition is in rather good agreement with the data of Thoma and Carlton [5]. Around 89% of the listed reflections are also present in our XRD data. Three polymorphs have been reported for $CsThF_5$ by Underwood et al. [37] from single crystal data: a tetragonal phase in space group $P4/nmm$, and two monoclinic phases in space groups $P2_1/c$. The phase obtained herein at room temperature was a mixture of tetragonal and monoclinic phases. The corresponding lattice parameters were determined with a Le Bail fit as $a = 5.725(5)$ Å, $c = 7.381(5)$ Å for the tetragonal phase, and $a = 8.325(5)$ Å, $b = 14.623(5)$ Å, $c = 8.500(5)$ Å, $\beta = 102.84(1)$ for the monoclinic phase, in reasonable agreement with the literature data of [37]. The DSC experimental data suggest only one transition at 942.7 K, however. The structure of the two monoclinic phases being very similar (both in space group $P2_1/c$), the corresponding transition entropy and transition enthalpy are probably too small to be detected. The model therefore reproduces only one transition.

The $(CsF:ThF_4) = (2:1)$, i.e., Cs_2ThF_6, composition gave an experimental XRD pattern in reasonable agreement with the data of Thoma and Carlton [5]. Around 73% of the listed reflections match our experimental pattern. The symmetry for this phase has not been reported in the literature, and a structural analogue could not be found.

The XRD pattern for the $(CsF:ThF_4) = (3:1)$, i.e., Cs_3ThF_7, composition is similar to that of the $(CsF:ThF_4) = (2:1)$ composition, as shown in Fig. 7, except for the intense reflections at 44.7°, 51.5°, 76.3°, 92.7°, 98.5°. Again the structure for this phase has not been reported in the literature. Thoma and Carlton [5] suggest a cubic symmetry with cell parameter $a = 9.659$ Å, but the space group and atomic positions have not been reported.

The present XRD data have hence confirmed the stability of five phases at room temperature: $CsTh_6F_{25}$, $Cs_2Th_3F_{14}$, $CsThF_5$, Cs_2ThF_6 and Cs_3ThF_7. Surprisingly, the $(CsF:ThF_4) = (1:3)$ composition did not match the structure reported by Underwood *et al.* [35,36,37] for the $CsTh_3F_{13}$ phase. The reasons for this discrepancy are unclear. Finally, the present results have confirmed that $CsTh_2F_9$ is not stable at room temperature.

4.3. $CsF–ThF_4$ phase diagram

Fig. 8 shows the optimized phase diagram of the $CsF\text{-}ThF_4$ system with the measured equilibrium points and the literature data points obtained from Thoma and Carlton [5]. Seven intermediate phases were identified, as in the work of Thoma and Carlton [5]: Cs_3ThF_7, Cs_2ThF_6, $CsThF_5$ (α and β phases), $Cs_2Th_3F_{14}$, $CsTh_2F_9$, $CsTh_3F_{13}$ and $CsTh_6F_{25}$.

The liquidus line is well represented in the whole composition range with regards to the measured equilibrium points. The α/β transition of $CsThF_5$ compound is also demonstrated, although there is a suggestion that there might be another transition in the $Cs_2Th_3F_{14}$ phase or a lower stability limit of the $CsTh_3F_{13}$ phase.

Three eutectics and four peritectics were found. The invariant equilibria in the $CsF–ThF_4$ system taken from the optimized phase diagram with the exact compositions and temperatures are listed in Table 5. The two intermediate compounds Cs_3ThF_7 and Cs_2ThF_6 melt congruently at 1251.8 K and 1155.9 K, respectively. The other

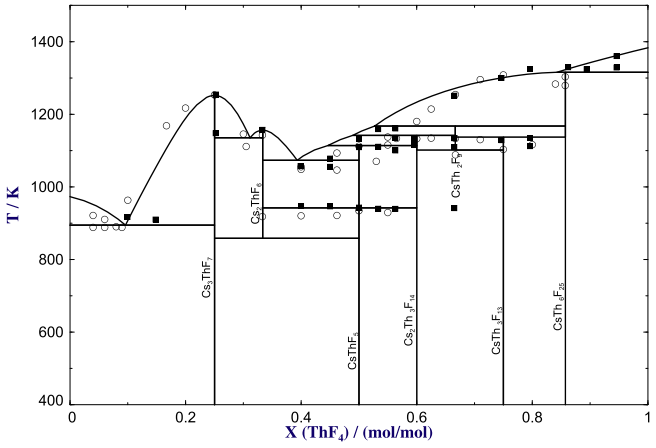

Fig. 8. Optimized phase diagram of the $CsF\text{-}ThF_4$ system with the measured equilibrium points (squares) and literature points (circles).

Table 5
The Invariant equilibria in the *CsF*–ThF_4 system at pressure p = 0.1 MPa. X ThF_4 is the molar fraction of ThF_4 and T is the absolute temperature in K. The standard uncertainties u are u(X) = 0.001, u(T) = 10 K, u(p) = 10 kPa.

X ThF_4/(mol/mol)	T/K	Type of Equilibrium
0.096	894.7	Eutectic
0.25	1251.8	Congruent melting point
0.31	1136	Eutectic
0.33	1155.9	Congruent melting point
0.393	1072.9	Eutectic
0.449	1113.9	Peritectic
0.489	1141.8	Peritectic
0.527	1167.6	Peritectic
0.667	1101.5	Lower limit of stability of phase $CsTh_2F_9$
0.75	1137.2	Upper limit of stability of phase $CsTh_3F_{13}$
0.84	1315.7	Peritectic

four compounds: β-$CsThF_5$, $Cs_2Th_3F_{14}$, $CsTh_3F_{13}$ and $CsTh_6F_{25}$ melt incongruently at 1113.9 K, 1141.8 K, 1137.2 K and 1315.7 K, respectively. The compound $CsTh_2F_9$ decomposes into $Cs_2Th_3F_{14}$ and $CsTh_3F_{13}$ upon cooling at 1101.5 K and has an upper limit of stability at the peritectic temperature of 1167.6 K. The lowest melting point was found at the eutectic point of 0.096 mol/mol of ThF_4 with the temperature of 894.7 K. The Cs_2ThF_6 phase was found stable at room temperature according to the XRD data, although this is not the case in the model, which is due to optimized enthalpy and entropy data chosen for a better representation of the liquidus line and more accurate fit to the experimental data.

In general, there is a very good agreement between the optimized data and the experimental points. However, slight discrepancies between the literature data and the model occur. The eutectic points at X = 0.305 mol/mol and X = 0.40 mol/mol of ThF_4 are 30 K higher than in the literature data. Thoma and Carlton [5] also measured an eutectic equilibrium at X = 0.53 mol/mol of ThF_4, which is also suggested by the steeper liquidus line shown in the Fig. 8 in the vicinity of X = 0.60 mol/mol of ThF_4 considering the literature points, which was not seen in the DSC measurements performed in this work and a peritectic melting was suggested instead.

4.4. Vapour pressure

Knudsen effusion mass spectrometry has been used in this work to investigate the vapour pressure over the molten CsF-ThF_4 salt, and further to determine the thermodynamic activities of the CsF and ThF_4 species in the liquid solution for the first time. The vapour pressure was investigated using three samples having compositions X = (0.4, 0.6 and 0.8) mol/mol of ThF_4 in order to understand the behaviour over the whole composition range. X = 0.2 mol/mol of ThF_4 could not be investigated due to its very high melting point of 1250 K. Hence at the experimental conditions the caesium fluoride completely evaporates before this temperature is reached. The resulting vapour pressures were compared to the vapour pressures of the pure CsF and ThF_4 compounds in the liquid phases, and the activities of species were calculated using the relation in Eq. 18.

$$a_i = \frac{P_i(Solution)}{P_i(Pure)}, \tag{18}$$

in which P_i (Solution) is the vapour pressure of the species *i* in the solution and P_i (Pure) is the vapour pressure of the end-member species *i*.

Since no experimental data exist for the ionization cross sections of the species studied in this work (ThF_4 and CsF), these were calculated using the approach of Deustch et al. [24] and are reported in Table 6, along with the atomic radii of mixed ions, their effective number of electrons and atomic ionization cross sections used for molecular cross section determination.

4.4.1. Vapour pressure of ThF_4

The measurement of pure ThF_4 was performed in our earlier work by Capelli et al. [15]. However, the analysis was repeated using the cross section from Table 6 evaluated using the method of Deutsch et al. [24] instead of the additive rule of Otvos and Stevenson [22]. Furthermore, the approximation of Grimley [18] based on Eq. (6) was used. The observed ionized species were ThF^{3+}, ThF^{2+}, ThF^+ and Th^+. The composition of the vapour consisted only of ThF_4 gas in the monomeric form, which was confirmed by the measured appearance potential curve. Fig. 9 shows the measured vapour pressure of pure ThF_4 and calculated values using the thermodynamic functions listed in Table 2 for comparison, showing a very good agreement between the measurement and the calculation.

4.4.2. Vapour pressure of CsF

The species considered in the measurement of pure cesium fluoride were $Cs_2F_2^+$, Cs_2F^+, CsF_2^+, Cs_2^+, Cs^+ and CsF^+. During the measurement, two appearance potential curves were obtained at fixed temperature and one is shown in Fig. 10. The Cs^+ signal reveals two inflections, indicating that the signal comes from three gaseous species: Cs(g), CsF(g) and Cs_2F_2(g). Substantial dissociation of Cs^+ from Cs_2F_2 dimer was confirmed by Roki et al. [38]. The $Cs_2F_2^+$, CsF^+ and CsF_2^+ ion signals are not displayed due to their low intensities in the order of magnitude of 10^{-11}. From the appearance potential curve (Fig. 10), the degree of Cs^+ dissociation was assessed and further used for the correct determination of the partial vapour pressure of the Cs-bearing species. CsF^+ signal comes fully from CsF gas, likewise for the dimer, Cs_2^+, Cs_2F^+, $Cs_2F_2^+$ and CsF_2^+ signals come each 100% from Cs_2F_2 gas.

Based on these obtained dissociation constants, the resulting pressure of the dimer Cs_2F_2 shows a very good agreement with the calculated values of the dimer pressure, obtained using the thermodynamic functions for the gaseous species listed in Table 2. Fig. 11 shows the measured, calculated and literature data [39,40,41] of pure CsF pressure for comparison. It can be noted that the contribution of the dimer to the total pressure is quite significant. The measured pressure of CsF(g) is slightly below the calculated values but in good agreement with the literature data [39,40,41].

4.4.3. Vapour pressure of the (Cs,Th) F_x

The mass spectrometry data of the liquid solution showed the presence of the following ions, Cs^+, CsF^+, Cs_2F^+, CsF_2^+, Th^+, ThF^+, ThF_2^+, ThF_3^+, ThF_4^+ for all three samples with different relative intensities. The maximum temperature reached during all measurements was 1600 K, at which point the salt and reference materials are completely vaporised. All the data have been analysed using the approach described in Section (2.4.1) with cross sections taken from Table 6.

A pre-melting treatment in an oven in a closed crucible was performed for the X = 0.4 mol/mol of ThF_4 composition as the first set of results obtained without a pre-melting treatment showed that CsF vaporized before the melting of the mixture due to the poor mixing in the solid state, thus shifting the composition.

Furthermore for each measurement, two sets of results were obtained, one calibrated on the silver pressure and one calibrated on the silver weight. These were averaged as they were in fair agreement and the deviation is shown as error. Fig. 12 shows the vapour pressure of one of the samples, X ThF_4 = 0.8 mol/mol, calibrated on the pressure of silver in comparison to pure ThF_4 and pure CsF vapour pressures. All intensities drop at the same

Table 6
Calculated ionization cross sections.

Species	Atomic radius/cm	Eff. number of electrons	Atomic Ion. cross Section (33.5 eV)/A^2	Calculated Ion. cross section/A^2
ThF_4	$19.37E^{-9}$/ $3.81E^{-9}$	12/7	16.6974/ 0.7329	7.05
Cs	$1.661E^{-8}$	9	10.1236	10.12
CsF	$1.661E^{-8}$/ $3.81E^{-9}$	9/7	10.1236/ 0.7329	6.45
Cs_2F_2	$1.661E^{-8}$/ $3.81E^{-9}$	9/7	10.1236/ 0.7329	12.9

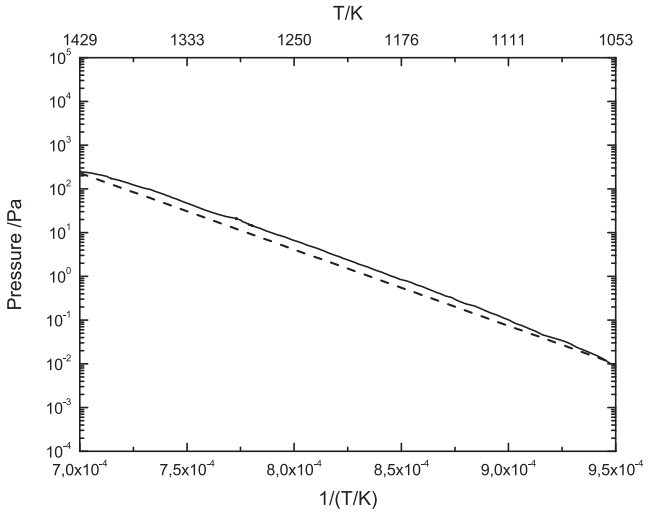

Fig. 9. Vapour pressure of pure *ThF*$_4$. (———) shows the measured values, (- - - - -) shows the calculated values.

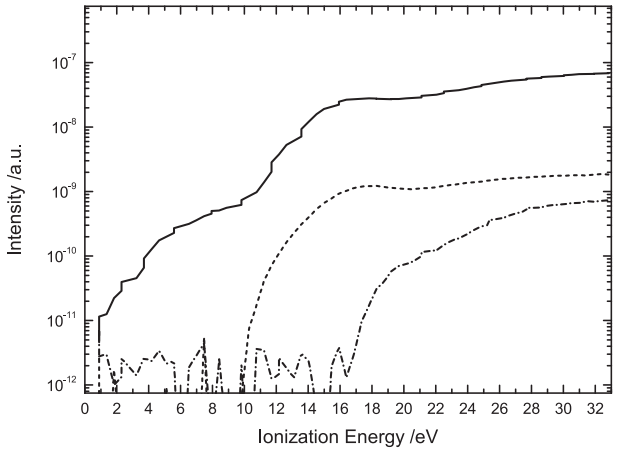

Fig. 10. Appearance potential curve of pure CsF for ions Cs^+, Cs_2^+ and Cs_2F^+. (———) shows the $^{133}Cs^+$ signal, (- - - - -) shows the $^{285}Cs_2F^+$ and (-·-·-·-) shows the $^{266}Cs_2^+$ signal.

temperature, suggesting correct mixing of the end-members. Furthermore, the pressures of CsF and ThF_4 in the mixture are below the pressures of pure CsF and ThF_4 respectively, which also confirms that the end-members are in the solution. The vapour pressure of the dimer Cs_2F_2 is quite significant but is not taken into account for the activities determination.

Fig. 13 shows the plot of the ThF_4 vapour pressures measured as a function of temperature for the different compositions in comparison to pure ThF_4 in the liquid phase. As expected the trend shows the highest pressure for the pure ThF_4 compound, decreasing with increasing CsF content.

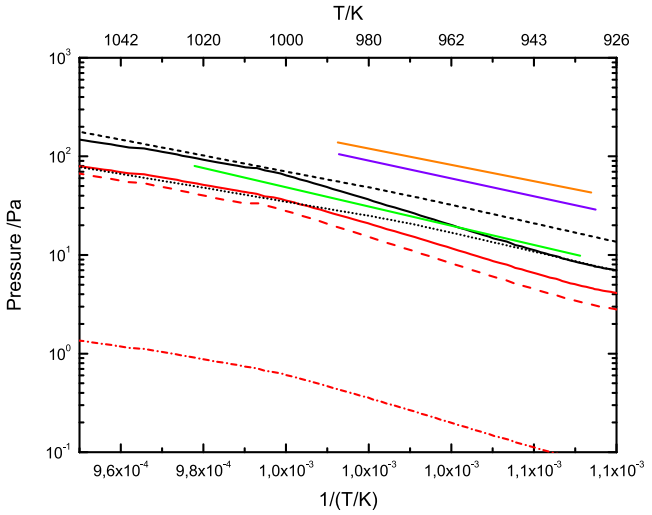

Fig. 11. Vapour pressure of pure CsF measured in this work in comparison with calculated data based on SGTE data [33] and data for CsF(g) from Pugh and Barrow [39] ———, Scheer et al. [40] ——— and Eisenstadt et al. [41] ———. (. . . . . .) shows the calculated vapour pressure of Cs_2F_2(g), (- - - -) shows the calculated vapour pressure of CsF(g), (———) shows the total vapour pressure, ——— shows the the vapour pressure of CsF(g), - - - - - shows the vapour pressure of Cs_2F_2(g) and -·-·-·- shows the vapour pressure of Cs(g).

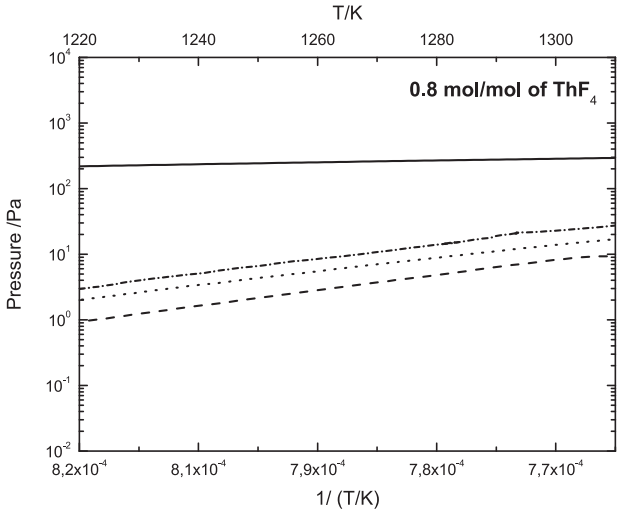

Fig. 12. Vapour pressure of the CsF-ThF_4 (0.2-0.8) mol/mol mixture. (———) shows the vapour pressure of pure CsF, (-·-·-·-) shows the vapour pressure of pure ThF_4, (· ·· · · ·) shows the vapour pressure of ThF_4 in the solution and (- - - - -) shows the vapour pressure of CsF in the solution.

Fig. 14 and Fig. 15 show the activities plots of the CsF (squares) and ThF_4 (circles) end-members in the liquid solution for two different temperatures, 1350 K and 1400 K. The activities were obtained from exact vapour pressure values at selected temperatures rather than from a fit. ThF_4 melts at 1384 K and therefore

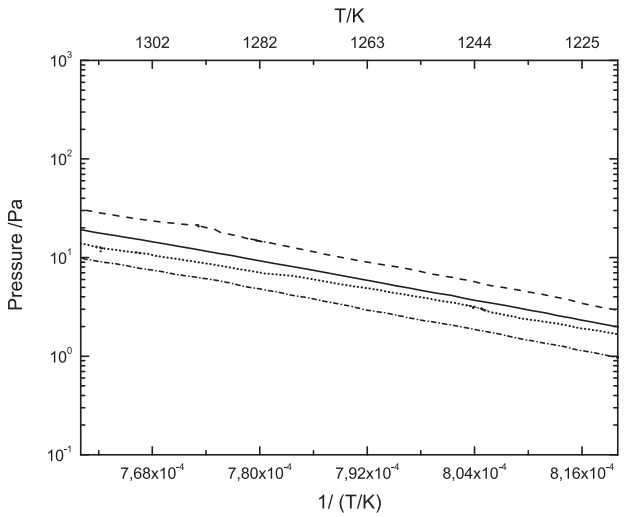

Fig. 13. Vapour pressures of ThF_4 in liquid solution of all samples in comparison to vapour pressure of pure *ThF_4* in the liquid phase. (– – – – –) shows the vapour pressure of pure ThF_4, (———) shows the vapour pressure of 0.8 mol/mol of ThF_4 in the liquid solution, (. . . . . .) shows the vapour pressure of 0.6 mol/mol of ThF_4 in the liquid solution and (– · – · – · –) shows the vapour pressure of 0.4 mol/mol of ThF_4 in the liquid solution.

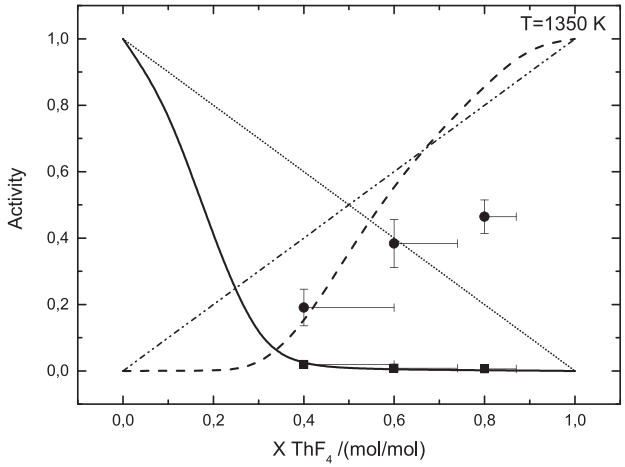

Fig. 14. Activities of CsF (squares) and ThF_4 (circles) in the liquid solution as a function of ThF_4 molar fraction at 1350 K. (———) shows the calculated activity of the CsF based on the developed thermodynamic model. (– – – – –) shows the calculated activity of ThF_4 based on the developed thermodynamic model. (. . . . . .) shows the Raoult's law for CsF and (– · – · – · –) shows the Raoult's law for ThF_4.

the reference state (pure ThF_4) at 1350 K refers to the supercooled state and is evaluated from the extrapolation of the fit of the vapour pressure in the liquid phase, which is given by Eq. 19 for the temperature range of 1384 K-1445 K.

$$\ln P/Pa = (24.75 \pm 0.29) - (27419 \pm 415) \cdot 1/(T/K) \quad (19)$$

The horizontal error bars were obtained from the calculation of the amount of CsF and ThF_4, which had evaporated up to the chosen temperatures for the activities using Eq. (8), therefore causing a shift in the composition and thus are suggested as composition uncertainties.

The vertical error bars are as mentioned before due to different ways of calculating the pressures using weight and pressure calibration factors of silver. Furthermore, each graph shows the predicted activities from the optimized thermodynamic model. The additional diagonal lines in the figures represent the behaviour of

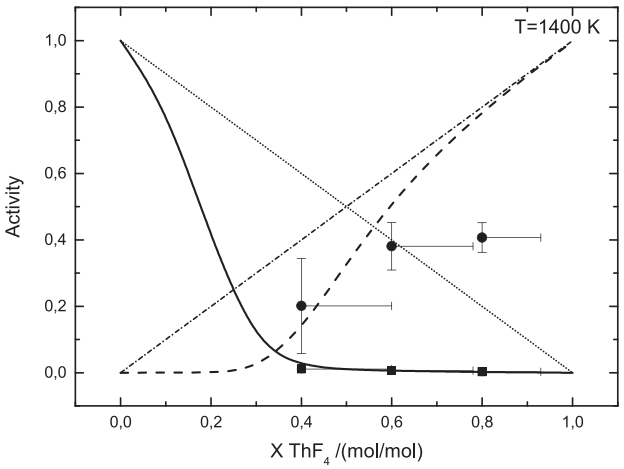

Fig. 15. Activities of CsF (squares) and ThF_4 (circles) in the liquid solution as a function of ThF_4 molar fraction at 1400 K. (———) shows the calculated activity of the CsF based on the developed thermodynamic model. (– – – – –) shows the calculated activity of ThF_4 based on the developed thermodynamic model. (. . . . . .) shows the Raoult's law for CsF and (– · – · – · –) shows the Raoult's law for ThF_4.

the activities for an ideal solution, given by Raoult's law ($a_i = X_i$), where X_i is the molar fraction of the gaseous species *i*.

The results show a strong negative deviation from the ideality of the liquid solution, particularly in the case of CsF. Overall, for CsF, the experimental and calculated values are in very good agreement. The calibration error bars for CsF are not visible as the values of the activities are very low, and so are the deviations due to the calibration. In the case of ThF_4, taking the calibration error into account, the measured and calculated values are in good agreement for the intermediate composition of X ThF_4 = 0.4 mol/mol and in reasonable agreement for the intermediate composition of X ThF_4 = 0.6 mol/mol. The measurement of the composition X ThF_4 = 0.8 mol/mol shows a strong deviation from the calculated values, which, however, is especially visible at increasing temperature.

Considering the composition shift, a strong error is apparent, mainly for the low concentration of X ThF_4 = 0.4 mol/mol and overall increasing at higher temperatures. Taking into account that the only available experimental data for the thermodynamic assessment of the binary system were the equilibrium data points, it can be concluded that the agreement between the values predicted by the model and the activities from the experiment is good indicating the same deviation from ideal behaviour.

5. Conclusion

A full thermodynamic assessment of the CsF-ThF_4 binary system is reported in the present work. Experimental phase diagram data were obtained using the DSC technique combined with post-characterization by powder X-ray diffraction. These data have provided the basis for the development of a thermodynamic model using the Factsage software and quasi-chemical model of Pelton [31]. The optimized phase diagram in this study consists of 9 invariant equlibria: 3 eutectics, 4 peritectics and 2 congruent melting points. 7 intermediate compounds were identified. The lowest melting temperature (894.7 K) was found at the eutectic point of 0.096 mol/mol of ThF_4. Furthermore, the measurement of the thermodynamic activities of ThF_4 and CsF in the liquid solution is reported for the first time. Knudsen effusion mass spectrometry has been applied to measure the vapour pressures in the CsF-ThF_4 system. The vaporising behaviour of pure CsF end-member

was firstly investigated, while the vaporising behaviour of pure ThF_4 was obtained from the literature and re-evaluated. The resulting vapour pressure of pure CsF was found in good agreement with the literature. Next, the vapour pressures of three different compositions were determined applying the same experimental conditions. Based on these measurements, the activity coefficients of the CsF and ThF_4 species in the liquid solution were obtained. The results have confirmed the same trends as the thermodynamic model and thus the reliability of the developed database. It can be concluded that CsF in the liquid solution has low vapour pressure leading to high CsF retention ability in the molten salt.

Acknowledgements

N.Vozárová acknowledges the European Commission for support given in the frame of the "Gentle" program. N.Vozárová acknowledges ETH for the support given within the Nuclear Engineering Master program. A.L. Smith acknowledges gratefully financial support from the Netherlands Organisation for Scientific Research (NWO) (project 722.016.005) and the Actinide User Laboratory programme for access to the experimental facilities of the Joint Research Centre Karlsruhe.

Appendix A. Appendix

This section shows the fits of the vapour pressure data of CsF and ThF_4 respectively, for 3 mentioned compositions, X = (0.8, 0.6, 0.4) mol/mol of ThF_4, all calibrated on pressure of silver, with their respective uncertainties and temperature validity ranges, along with the fits of pure ThF_4 and pure CsF. Tables A1–A9 show the measured vapour pressure data, calibrated on vapour pressure of silver and on weight of silver with their respective uncertainties.

Pure CsF.

$$\ln P/Pa = (18.9 \pm 0.2) - (15294 \pm 208) \cdot 1/(T/K) \quad T = 1009K - 1052K \tag{20}$$

$$\ln P/Pa = (31.7 \pm 0.08) - (28154 \pm 85) \cdot 1/(T/K) \quad T = 928K - 998K \tag{21}$$

Pure ThF_4.

$$\ln P/Pa = (33.97 \pm 0.13) - (40217 \pm 169) \cdot 1/(T/K) \quad T = 1037K - 1445K \tag{22}$$

ThF_4 in X = 0.8 mol/mol of ThF_4 solution.

$$\ln P/Pa = (31.93 \pm 0.14) - (38290 \pm 171) \cdot 1/(T/K) \quad T = 1017K - 1408K \tag{23}$$

CsF in X = 0.8 mol/mol of ThF_4 solution.

$$\ln P/Pa = (20.54 \pm 0.22) - (22835 \pm 249) \cdot 1/(T/K) \quad T = 998K - 1207K \tag{24}$$

ThF_4 in X = 0.6 mol/mol of ThF_4 solution.

$$\ln P/Pa = (29.88 \pm 0.08) - (35882 \pm 102) \cdot 1/(T/K) \quad T = 985K - 1402K \tag{25}$$

CsF in X = 0.6 mol/mol of ThF_4 solution.

$$\ln P/Pa = (17.3 \pm 0.13) - (18975 \pm 152) \cdot 1/(T/K) \quad T = 990K - 1235K \tag{26}$$

$$\ln P/Pa = (18.7 \pm 0.13) - (21490 \pm 183) \cdot 1/(T/K) \quad T = 1311K - 1374K \tag{27}$$

ThF_4 in X = 0.4 mol/mol of ThF_4 solution.

$$\ln P/Pa = (34.59 \pm 0.15) - (42446 \pm 191) \cdot 1/(T/K) \quad T = 1038K - 1400K \tag{28}$$

CsF in X = 0.4 mol/mol of ThF_4 solution.

$$\ln P/Pa = (19.74 \pm 0.25) - (20140 \pm 287) \cdot 1/(T/K) \quad T = 953K - 1309K \tag{29}$$

Appendix B. Supplementary data

Supplementary data associated with this article can be found, in the online version, at http://dx.doi.org/10.1016/j.jct.2017.05.008.

References

[1] Gen. IV International Forum Portal, 2016. <http://www.gen-4.org> [Accessed 13 Jun. 2016].
[2] Thorium – World Nuclear Association, 2016. World-nuclear.org [Accessed 20 Jun. 2016].
[3] S. Delpech, E. Merle-Lucotte, D. Heuer, M. Allibert, V. Ghetta, C. Le-Brun, X. Doligez, G. Picard, Reactor physic and reprocessing scheme for innovative molten salt reactor system, J. Fluorine Chem. 130 (2009) 11–17.
[4] J. Petruska, E. Melaika, R. Tomlinson, The fission yields of the cesium isotopes formed in the thermal neutron fission of U 235 and the neutron absorption cross section of Xe 135, Can. J. Phys. 33 (1955) 640–649.
[5] R. Thoma, T. Carlton, Phase equilibria in the system CsF—ThF4, J. Inorg. Nucl. Chem. 17 (1961) 88–97.
[6] P. Souček, O. Beneš, B. Claux, E. Capelli, M. Ougier, V. Tyrpekl, J.F. Vigier, J.M. Konings, Synthesis of UF4 and ThF4 by HF gas fluorination and re-determination of the UF4 melting point *FLUOR* – 2017 – 126, J. Fluorine Chem. (2017).
[7] R. Lindstrom, W. Ellis, Kinetics of the hydrofluorination of thorium dioxide, J. Chem. Phys. 43 (3) (1965) 994.
[8] W.J. Asker, E.R. Segmit, A.W. Wylie, The potassium thorium fluorides, J. Chem. Soc. (1973) 4470.
[9] W. Steinmann, G. Seide, M. Beckers, S. Walter, T. Gries, Thermal Analysis of Phase Transitions and Crystallization in Polymeric Fibers, NTECH Open Access Publisher, 2013.
[10] A. Elkordy, Applications of calorimetry in a wide context, Intech, Rijeka, Croatia, 2013.
[11] O. Beneš, R. Konings, S. Wurzer, M. Sierig, A. Dockendorf, A DSC study of the $NaNO_3$—KNO_3 system using an innovative encapsulation technique, Thermochim. Acta 509 (1–2) (2010) 62–66.
[12] J. Rodriguez-Carvajal, Recent advances in magnetic structure determination by neutron powder diffraction, Phys. B 192 (1993) 55–69.
[13] J. Hiernaut, J.-Y. Colle, R. Pflieger-Cuvellier, J. Jonnet, J. Somers, C. Ronchi, A Knudsen cell-mass spectrometer facility to investigate oxidation and vaporisation processes in nuclear fuel, J. Nucl. Mater. 344 (1–3) (2005) 246–253.
[14] J.-Y. Colle, KEMS Technique – Knudsen Effusion Mass Spectrometry (KEMS-online), 2016. <https://sites.google.com/site/kemsonline/the-technique> [Accessed 13 Jun. 2016]
[15] E. Capelli, O. Beneš, J. Colle, R. Konings, Determination of the thermodynamic activities of LiF and ThF4 in the $Li_xTh_{1-x}F_{4-3x}$ liquid solution by Knudsen effusion mass spectrometry, Phys. Chem. Chem. Phys. 17 (44) (2015) 30110–30118.
[16] P. Gotcu-Freis, J.-Y. Colle, J. Hiernaut, F. Naisse, C. Gueneau, R. Konings, Mass spectrometric studies of the vapour phase in the (Pu+O) system, J. Chem. Thermodyn. 43 (8) (2011) 1164–1173.
[17] J. Margrave, R. Hultgren, Selected values of thermodynamic properties of metals and alloys, J. Chem. Educ. 41 (2) (1964) 114.
[18] R. Grimley, J. Forsman, Q. Grindstaff, A mass spectrometric study of the fragmentation of the lithium fluoride vapor system, J. Phys. Chem. 82 (6) (1978) 632–639.
[19] J. Mann, Ionization cross sections of the elements calculated from mean-square radii of atomic orbitals, J. Chem. Phys. 46 (5) (1967) 1646.
[20] J. Mann, K. Ogata. Recent developments in mass spectrometry, in: Proceedings of the Conference on Mass Spectroscopy, 1970.
[21] D. Bonnell, J. Hastie, Program SIGMA, A Fortran code for computing atomic ionisation cross-sections (n.d.).
[22] J. Otvos, D. Stevenson, Cross-sections of molecules for ionization by electrons, J. Am. Chem. Soc. 78 (3) (1956) 546–551.
[23] J. Desclaux, Relativistic Dirac-Fock expectation values for atoms with Z = 1 to Z = 120, At. Data Nucl. Data Tables 12 (4) (1973) 311–406.
[24] H. Deutsch, K. Becker, T. Märk, A modified additivity rule for the calculation of electron impact ionization cross-section of molecules AB_n, Int. J. Mass Spectr. Ion Processes 167–168 (1997) 503–517.
[25] M. Cardona, L. Ley, Photoemission in Solids I: General Principles, Springer-Verlag, Berlin, 1978.
[26] J.A. Bearden, A.F. Burr, Reevaluation Of X-Ray Atomic Energy Levels, Rev. Modern Phys. 39 (1967) 125–142.

[27] J.C. Fuggle, N. Martensson, Core-level binding energies in metals, J. Electron Spectrosc. Relat. Phenom. 21 (1980) 275.
[28] S. Yang, M. Jiang, H. Li, Y. Liu, L. Wang, Assessment of Co-Cr-Ni ternary system by CALPHAD technique, Rare Metals 31 (1) (2012) 75–80.
[29] L. Kaufman, H. Bernstein, Computer Calculations of Phase Diagrams, Academic Press, New York, 1970.
[30] J. Leitner, P. Voňka, D. Sedmidubský, P. Svoboda, Application of Neumann-Kopp rule for the estimation of heat capacity of mixed oxides, Thermochim. Acta 497 (1–2) (2010) 7–13.
[31] A. Pelton, P. Chartrand, G. Eriksson, The modified quasi-chemical model: Part IV. Two-sublattice quadruplet approximation, Metall. Mater. Trans. A 32 (6) (2001) 1409–1416.
[32] E. Capelli, O. Beneš, M. Beilmann, R. Konings, Thermodynamic investigation of the LiF-ThF4 system, J. Chem. Thermodyn. 58 (2013) 110–116.
[33] K. Hack, (Ed.). The SGTE-Casebook - Thermodynamics at work The Institute of Materials, Materials Modelling Series, ISBN 0 901716 74X, 1996.
[34] J. Sangster, Thermodynamics and Phase Diagrams of 32 Binary Common-Ion Systems of the Group Li, Na, K, Rb, Cs//F, Cl, Br, I, OH, NO3, J. Phase Equilibr. 21 (3) (2000) 68–241.
[35] C.C. Underwood, C.D. McMillen, J.W. Kolis, The crystal structures of CsTh6F25 and NaTh3F13, J. Chem. Crystallogr. 42 (2012) 606–610.
[36] C.C. Underwood, M. Mann, C.D. McMillen, J.W. Kolis, Hydrothermal descriptive chemistry and single crystal structure determination of cesium and rubidium thorium fluorides, Inorg. Chem. 50 (2011) 11825–11831.
[37] C.C. Underwood, M. Mann, C.D. McMillen, J.D. Musgraves, J.W. Kolis, The polymorphism of CsThF5, Solid State Sci. 14 (2012) 574–579.
[38] F. Roki, M. Ohnet, S. Fillet, C. Chatillon, I. Nuta, Critical assessment of thermodynamic properties of CsI solid, liquid and gas phases, J. Chem. Thermodyn. 70 (2014) 46–72.
[39] A. Pugh, R. Barrow, The heats of sublimation of inorganic substances. Part 5. – The alkali metal fluorides, Trans. Faraday Soc. 54 (1958) 671–678.
[40] M. Scheer, J. Fine, Entropies, heats of sublimation, and dissociation energies of the cesium halides, J. Chem. Phys. 36 (6) (1962) 1647.
[41] M. Eisenstadt, G. Rothberg, P. Kusch, Molecular composition of alkali fluoride vapors, J. Chem. Phys. 29 (4) (1958) 797.